

Orbital Ordering and Magnetic Interactions in BiMnO_3

I V Solovyev¹, Z V Pchelkina²

¹ Computational Materials Science Center, National Institute for Materials Science, 1-2-1 Sengen, Tsukuba, Ibaraki 305-0047, Japan

E-mail: solovyev.igor@nims.go.jp

² Institute of Metal Physics, Russian Academy of Sciences – Ural Division, 620041 Ekaterinburg GSP-170, Russia

Abstract. This work is devoted to the analysis of orbital patterns and related to them interatomic magnetic interactions in centrosymmetric monoclinic structures of BiMnO_3 , which have been recently determined experimentally. First, we set up an effective lattice fermion model for the manganese $3d$ bands and derive parameters of this model entirely from first-principles electronic structure calculations. Then, we solve this model in terms of the mean-field Hartree-Fock method and derive parameters of interatomic magnetic interactions between Mn ions. We argue that although nearest-neighbor interactions favors the ferromagnetism, they compete with longer-range antiferromagnetic (AFM) interactions, the existence of which is directly related with the peculiar geometry of the orbital ordering pattern realized in BiMnO_3 below 474 K. These AFM interactions favor an AFM phase, which breaks the inversion symmetry. The formation of the AFM phase is assisted by the orbital degrees of freedom, which tend to adjust the nearest-neighbor magnetic interactions in the direction, which further stabilizes this phase. We propose that the multiferroelectric behavior, observed in BiMnO_3 , may be related with the emergence of the AFM phase under certain conditions.

PACS numbers: 75.30.-m, 77.80.-e, 75.47.Lx, 75.10.Lp

1. Introduction

The multiferroic compounds have recently drawn an enormous attention due to promising practical applications as well as the fundamental interest [1, 2, 3, 4]. Such systems, where magnetism coexists with the ferroelectricity, could be potentially used in the new devices aiming to transform the information in the form of the magnetization into the electric voltage and back. The primary goal of theorists is to unveil the microscopic mechanism leading to the coupling between magnetic and electric degrees of freedom.

The bismuth manganite (BiMnO_3), having highly distorted perovskite structure, has been regarded as one of the prominent multiferroic materials. Indeed, the ferromagnetism of BiMnO_3 is well established today. The Curie temperature (T_C) is

about 100 K. The largest reported saturation magnetization is $3.92 \mu_B$ per one formula unit [5],¹ which is close to $4 \mu_B$ expected for the fully saturated ferromagnetic (FM) state. Nevertheless, the saturation magnetization decreases rapidly with the doping in $\text{Bi}_{1-x}\text{Sr}_x\text{MnO}_3$ [6], that may indicate at the proximity of yet another and apparently antiferromagnetic (AFM) phase.

However, the situation around the ferroelectric properties of BiMnO_3 is more controversial. There are several facts, which do support the idea that BiMnO_3 is not only ferromagnetic, but also a ferroelectric material.

- (i) The existence of ferroelectricity has been advocated by first-principles electronic structure calculations [7], and attributed to the chemical activity of the $\text{Bi}(6s^2)$ lone pairs [8], in an analogy with other ferroelectric materials, such as PbTiO_3 .
- (ii) According to early experimental data from electron and neutron powder diffraction, BiMnO_3 was considered to have noncentrosymmetric $C2$ space group in the entire monoclinic region [9, 10], which is consistent with the ferroelectric behavior. Namely, BiMnO_3 undergoes two phase transitions at the temperatures of 474 and 770 K [9, 10]. The first one at 474 K takes place without changing the monoclinic symmetry [11]. The phase transition at 770 K is monoclinic to orthorhombic [11] and was believed likely to be ferroelectric-paraelectric. Nevertheless, it is also worth to note that this point of view is rather controversial and according to [12] the onset of the ferroelectric behavior is expected only around 450 K, which in [12] was the point of isostructural (i.e., monoclinic to monoclinic) phase transition.
- (iii) The ferroelectric hysteresis loop has been also reported in polycrystalline and thin film samples of BiMnO_3 [12], although the measured ferroelectric polarization was small (about $0.043 \mu\text{C}/\text{cm}^2$ at 200 K). The first principle calculations performed for the experimental noncentrosymmetric structure result in much higher polarization (about $0.52 \mu\text{C}/\text{cm}^2$) [13].
- (iv) Kimura *et al.* [14] observed the changes of the dielectric constant induced by the magnetic ordering as well as by the external magnetic field near $T_C \sim 100$ K, and attributed them to the multiferroic behavior of BiMnO_3 .
- (v) Sharan *et al.* [15] observed the electric-field-induced permanent changes in the second harmonic response from the BiMnO_3 thin film, and argued that these changes are consistent with the possible presence of ferroelectricity.

However, there is also a growing evidence against the intrinsic ferroelectric behavior of BiMnO_3 .

- (i) Recently the crystal structure of BiMnO_3 was reexamined by Belik *et al.* [5]. After careful analysis, they concluded that both monoclinic phases observed in BiMnO_3 below 770 K have *centrosymmetric* space group $C2/c$. If so, BiMnO_3 should be an *antiferroelectric*, rather than the ferroelectric material. This finding was further confirmed in the neutron powder diffraction experiments by Montanari

¹ measured at the temperature of 5 K and in the magnetic field of 5 T.

et al. [16] who also concluded that the crystal structure of BiMnO_3 is better described by the $C2/c$ group in the wide range of temperatures ($10 \leq T \leq 295$ K) and magnetic fields ($0 \leq H \leq 10$ T). It is also important to note that there are many objective difficulties in the determination of the crystal structure of BiMnO_3 , which are mainly related with the strong effect of nonstoichiometry [17].²

- (ii) For the related compound BiScO_3 , both neutron powder and electron diffraction analysis result in the centrosymmetric $C2/c$ space group [19].
- (iii) The structure optimization performed by using modern methods of electronic structure calculations revealed that the noncentrosymmetric $C2$ structure, which has been reported earlier [9, 10], inevitably converges to the new total energy minimum corresponding to the $C2/c$ structure with zero net polarization [20, 21].

The goal of this work is to study of the orbital ordering and corresponding to it interatomic magnetic interactions in the centrosymmetric structure of BiMnO_3 . For these purposes we construct an effective lattice fermion model and derive parameters of this model from first-principles electronic structure calculations. After solution of this model we calculate the interatomic magnetic interactions. We argue that the peculiar orbital ordering realized below 474 K gives rise to FM interactions between nearest-neighbor spins which always compete with longer-range AFM interactions. We propose that the ferroelectric behavior of BiMnO_3 can be related with the emergence of an AFM phase, which is stabilized by these longer-range interactions and breaks the inversion symmetry.

Thus, according to our point of view, the multiferroic behavior of BiMnO_3 is feasible and can be related with competition of two magnetic phases coexisting in a narrow energy range. The centrosymmetric FM ground state itself is antiferroelectric. Nevertheless, the ferroelectricity can be observed in the noncentrosymmetric AFM phase, which can apparently exist under certain conditions. Since the ferromagnetic (antiferroelectric) and antiferromagnetic (ferroelectric) phases can be stabilized by applying the magnetic and electric field, respectively, the magnetic moment can be switched off by the electric field and vice versa. This constitutes our idea of multiferroic behavior of BiMnO_3 . We rationalize several experimental facts on the basis of this picture.

The paper is organized as follows. In the next section we discuss details of the centrosymmetric crystal structure of BiMnO_3 . Section 3 briefly describes results of first principle electronic structure calculations in the local-density approximation (LDA). The construction of the model Hamiltonian is addressed in Section 4. The solution of the model Hamiltonian and physical meaning of interatomic magnetic interactions is discussed in Section 5. The results of calculations are discussed in Section 6. Finally, in Section 7 we will summarize our work and discuss how our results are related with the

² In fact, the experimental situation is complicated by the samples differences (thin films or bulk), nonstoichiometry, effect of substrate (for the thin films), etc. Some difficulties and artifacts arising in the experiment for multiferroic and magnetoelectric thin films have been discussed in [18].

observed experimental behavior of BiMnO_3 .

2. Crystal Structure and Symmetry Considerations

BiMnO_3 has a highly distorted perovskite structure (figure 1).

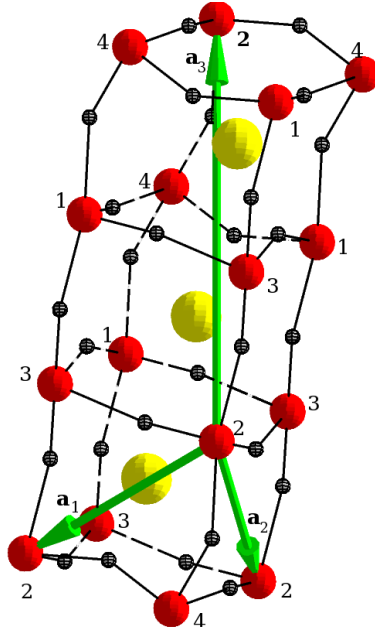


Figure 1. Fragment of crystal structure of BiMnO_3 , presented in the form of highly distorted perovskite lattice. The Bi atoms are indicated by the big yellow (light grey) spheres, the Mn atoms are indicated by the medium red (dark grey) spheres, and the oxygen atoms are indicated by the small hatched spheres. The primitive cell includes four Mn atoms, which are indicated by the numbers. The primitive translations are shown by arrows.

In our calculations we used the experimental crystal structure for $T = 4$ and 550 K obtained by Belik *et al.* The experimental structure parameters for $T = 550$ K can be found in [5], while the ones for $T = 4$ K are unpublished data [22].³ The primitive translations in the original monoclinic coordinate frame are give by

$$\mathbf{a}_1 = (4.4605, -2.8019, -1.6748)$$

$$\mathbf{a}_2 = (4.4605, 2.8019, -1.6748)$$

$$\mathbf{a}_3 = (0, 0, 9.8481)$$

(in Å, for $T = 4$ K).

³ The structure parameters for $T = 4$ K are pretty close to the ones for reported in [5] for $T = 300$ K. In fact, all calculations have been performed using the experimental crystal structure both for $T = 4$ K and $T = 300$ K. Since both structures produce similar results, in the following we consider only the case of $T = 4$ K.

The space group $C2/c$ has four symmetry operations:

$$\begin{aligned}\hat{S}_1 &= \{E|\mathbf{0}\} \\ \hat{S}_2 &= \{I|\mathbf{0}\} \\ \hat{S}_3 &= \{m_y|\mathbf{a}_3/2\} \\ \hat{S}_4 &= \{C_y^2|\mathbf{a}_3/2\},\end{aligned}\tag{1}$$

where in the notation $\{\mathcal{O}|\mathbf{t}\}$, $\mathcal{O} = E, I, m_y$, or C_y^2 denotes the local symmetry operation, which is combined with the translation $\mathbf{t} = \mathbf{0}$ or $\mathbf{a}_3/2$. Other notations are the following: E is the unity operation, I is the inversion, m_y is the mirror reflection of the axis y , and C_y^2 is the 180° rotation around y .

The primitive cell of BiMnO_3 has four formula units. Four Mn atoms are located at

$$\begin{aligned}\text{Mn1} &: (0, -1.2069, 2.4620) \\ \text{Mn2} &: (0, 1.2069, -2.4620) \\ \text{Mn3} &: (2.2303, -1.4009, -0.8374) \\ \text{Mn4} &: (2.2303, 1.4009, 4.0866)\end{aligned}$$

(in Å). They can be divided in two groups (Mn1, Mn2) and (Mn3, Mn4), so that in each group the atoms can be transformed to each other by the symmetry operations (1). The corresponding transformation law is given in table 1.

Table 1. The transformation law of four Mn atoms in BiMnO_3 under symmetry operations of the $C2/c$ group. Four Mn atoms are listed in the first column. Next four columns show their images after applying the symmetry operations of the $C2/c$ space group.

atom	$\{E \mathbf{0}\}$	$\{I \mathbf{0}\}$	$\{m_y \mathbf{a}_3/2\}$	$\{C_y^2 \mathbf{a}_3/2\}$
Mn1	Mn1	Mn2	Mn2	Mn1
Mn2	Mn2	Mn1	Mn1	Mn2
Mn3	Mn3	Mn3	Mn4	Mn4
Mn4	Mn4	Mn4	Mn3	Mn3

The ferromagnetic configuration of BiMnO_3 has the full $C2/c$ symmetry, which excludes any ferroelectricity. Possible antiferromagnetic configurations can be obtained by combining the symmetry operations (1) with the time-inversion \hat{T} , which flips directions of the magnetic moments. Then, one can expect the following possibilities:

- (i) The AFM configuration $\uparrow\uparrow\downarrow\downarrow$ (in these notations, four arrows correspond to the directions of the magnetic moments at the Mn-sites 1, 2, 3, and 4, respectively), which transforms according to the original space group $C2/c$. Similar to the FM case, this configuration exclude the ferroelectricity.
- (ii) The AFM configuration $\uparrow\downarrow\downarrow\uparrow$, which apart from the unity element $\{E|\mathbf{0}\}$, has only one symmetry operation: $\hat{T} \otimes \{m_y|\mathbf{a}_3/2\}$. This configuration does allow for the

ferroelectricity, and the spontaneous polarization is expected to be perpendicular to the y -axis. Once the symmetry is broken by the AFM order, the atomic position will shift in order to minimize the total energy via magneto-elastic interactions. In this case, the crystal symmetry is expected to be $P2$, which is compatible with the magnetic symmetry of the AFM $\uparrow\downarrow\downarrow\uparrow$ phase.⁴ Thus, the ferroelectric behavior in the $\uparrow\downarrow\downarrow\uparrow$ phase is driven by the magnetic breaking of the inversion symmetry. A similar scenario of appearance of the ferroelectricity has been recently considered for other manganese oxides: HoMnO_3 [23, 24] and TbMn_2O_5 [25].

Other combinations of \hat{T} with the symmetry operations (1) will lead to unphysical solutions, where the local magnetic moments will vanish in one of the Mn-sublattices. Although such configurations are formally allowed by the symmetry, they clearly conflict with intraatomic Hund's first rule and are expected to have much higher energy.⁵ We have also considered two ferrimagnetic configurations $\uparrow\downarrow\downarrow\downarrow$ and $\downarrow\downarrow\uparrow\downarrow$, which do not have any symmetry. In this case, the spontaneous polarization may have an arbitrary direction.

Below 474 K, the MnO_6 octahedra are strongly distorted. Around each Mn site, there are three inequivalent pairs of Mn-O bonds. At $T = 4$ K, the values of the Mn-O bondlengths are (1.899 Å, 1.997 Å, 2.189 Å) and (1.930 Å, 1.940 Å, 2.230 Å), around the sites Mn1 and Mn3, respectively. In the first approximation, one can say that there are four short Mn-O bonds and two long Mn-O bonds. This distortion leads to the preferential population of the e_g orbitals of the z^2 symmetry, aligned along the long Mn-O bonds. The difference between the longest and shortest Mn-O distances around the sites Mn1 and Mn3 is 0.290 Å and 0.300 Å, respectively. This distortion is substantially relieved above 474 K. For example, at $T = 550$ K, the Mn-O bondlengths around the sites Mn1 and Mn3 are (2.011 Å, 2.032 Å, 2.112 Å) and (1.913 Å, 2.024 Å, 2.106 Å), respectively, and the difference between the longest and shortest Mn-O distances around the sites Mn1 and Mn3 is reduced till 0.101 Å and 0.193 Å, respectively. Thus, the reduction is the most dramatic around the site Mn1.

3. Electronic Structure in the Local-Density Approximation

First, we calculate the electronic structure corresponding to the low and high temperature structure of BiMnO_3 in the local density approximation (LDA) by using linear-muffin-tin-orbital (LMTO) method [26, 27, 28]. The atomic spheres radii and some details of the LMTO basis set used in the calculation are given in table 2. In order to fill the unit cell volume and reduce the overlap between atomic spheres, we

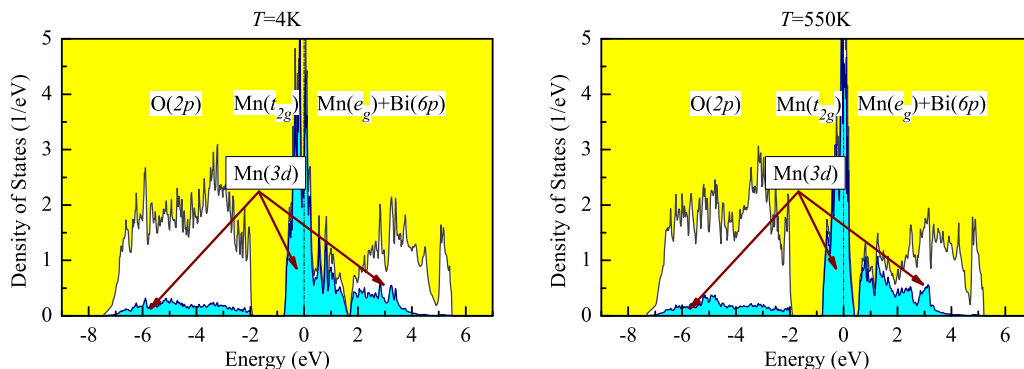
⁴ In the other words, the distribution of the *electron density* in the AFM $\uparrow\downarrow\downarrow\uparrow$ phase obeys the $P2$ group, while the distribution of the *magnetization density* obeys the magnetic group in which $\{m_y|\mathbf{a}_3/2\}$ is combined with \hat{T} .

⁵ Note that in manganites, the intraatomic exchange coupling J is about 0.9 eV and the local magnetic moment M is about $4\mu_B$. Therefore, the Hund energy, $-\frac{1}{4}JM^2$, is expected to be about 3.6 eV per one Mn site.

Table 2. Details of LMTO calculations for BiMnO_3 at 4 and 550 K. The notations of inequivalent oxygen atoms are the same as in [5].

type of atom	LMTO basis	radii (\AA)	
		4 K	550 K
Bi	$6s6p6d5f$	1.59	1.54
Mn1	$4s4p3d$	1.24	1.32
Mn3	$4s4p3d$	1.26	1.25
O1	$2s2p$	0.98	1.04
O2	$2s2p$	0.97	1.02
O3	$2s2p$	0.99	0.97

additionally introduced 36 and 42 empty spheres for the 4 K and 550 K structure, respectively. The resulting total and partial densities of state are shown in figure 2. The oxygen band, lying between -7 and -2 eV, is completely filled. The electronic

**Figure 2.** Total and partial densities of states as obtained for the low-temperature (left) and high-temperature (right) monoclinic structures of BiMnO_3 in the local-density approximation. The shaded area shows contributions of the manganese $3d$ states. Other symbols show the positions of the main bands. The Fermi level is at zero energy.

structure near the Fermi level is mainly formed by the $\text{Mn}(3d)$ states. Due to the hybridization, there is also a considerable weight of the $\text{Mn}(3d)$ states in the oxygen band. The electronic structure near the Fermi level is further split into the $\text{Mn}(e_g)$ and $\text{Mn}(t_{2g})$ bands by pseudocubic crystal field operating in the MnO_6 octahedra, although in the highly distorted monoclinic structure there is no unique definition of the “ t_{2g} ” and “ e_g ” orbitals since they are always mixed by the crystal distortion. The distortion is particularly strong in the low-temperature phase, leading even to an overlap between $\text{Mn}(t_{2g})$ and $\text{Mn}(e_g)$ bands. The $\text{Mn}(e_g)$ band itself is split into the low- and high-energy subbands, lying at around 1 eV and 3 eV, respectively. There is a small gap between these subbands at around 1.7 eV. In total, the low-energy $\text{Mn}(e_g)$ subband can accommodate one electron per one formula unit of BiMnO_3 . Therefore, according to the

formal valence argument, in the fully polarized FM phase, both $\text{Mn}(t_{2g})$ and low-energy $\text{Mn}(e_g)$ bands are expected to be filled for the majority-spin channel, and the Fermi level is expected to fall in the pseudogap. The crystal distortion is somewhat released in the high-temperature structure, that leads to the opening of a gap between $\text{Mn}(t_{2g})$ and $\text{Mn}(e_g)$ bands and closing the gap between two $\text{Mn}(e_g)$ subbands. The high-energy $\text{Mn}(e_g)$ subbands always overlap with the $\text{Bi}(6p)$ band spreading from about 2 to 5 eV. In this sense, any attempt to construct the model Hamiltonian for the isolated $\text{Mn}(3d)$ bands will be conjugated with some additional approximations for treating the $\text{Bi}(6p)$ states and their hybridization with the $\text{Mn}(3d)$ states.

4. Construction of the Model Hamiltonian

Our next goal is the construction of an effective multi-orbital Hubbard-type model for the $\text{Mn}(3d)$ bands, located near the Fermi level, and derivation of the parameters of this model from the first-principles electronic structure calculations. The method has been proposed in [29]. Many details can be found in the recent review article [30].

The model itself is specified as follows:

$$\hat{\mathcal{H}} = \sum_{\mathbf{R}\mathbf{R}'} \sum_{\alpha_1\alpha_2} t_{\mathbf{R}\mathbf{R}'}^{\alpha_1\alpha_2} \hat{c}_{\mathbf{R}\alpha_1}^\dagger \hat{c}_{\mathbf{R}'\alpha_2} + \frac{1}{2} \sum_{\mathbf{R}} \sum_{\{\alpha\}} U_{\alpha_1\alpha_2\alpha_3\alpha_4}^{\mathbf{R}} \hat{c}_{\mathbf{R}\alpha_1}^\dagger \hat{c}_{\mathbf{R}\alpha_3}^\dagger \hat{c}_{\mathbf{R}\alpha_2} \hat{c}_{\mathbf{R}\alpha_4}, \quad (2)$$

where $\hat{c}_{\mathbf{R}\alpha}^\dagger$ ($\hat{c}_{\mathbf{R}\alpha}$) creates (annihilates) an electron in the Wannier orbital $\tilde{W}_{\mathbf{R}}^\alpha$ centered at the Mn-site \mathbf{R} , and α is a joint index, incorporating spin ($s = \uparrow$ or \downarrow) and orbital ($m = xy, yz, z^2, zx$, or $x^2 - y^2$) degrees of freedom. The one-electron Hamiltonian $\hat{t}_{\mathbf{R}\mathbf{R}'}^{\alpha_1\alpha_2} = \|t_{\mathbf{R}\mathbf{R}'}^{\alpha_1\alpha_2}\|$ usually includes the following contributions: the site-diagonal part ($\mathbf{R} = \mathbf{R}'$) describes the crystal-field splitting, whereas the off-diagonal part ($\mathbf{R} \neq \mathbf{R}'$) stands for transfer integrals, describing the kinetic energy of electrons.

$$U_{\alpha_1\alpha_2\alpha_3\alpha_4}^{\mathbf{R}} = \int d\mathbf{r} \int d\mathbf{r}' \tilde{W}_{\mathbf{R}}^{\alpha_1\dagger}(\mathbf{r}) \tilde{W}_{\mathbf{R}}^{\alpha_2}(\mathbf{r}) v_{\text{scr}}(\mathbf{r}, \mathbf{r}') \tilde{W}_{\mathbf{R}}^{\alpha_3\dagger}(\mathbf{r}') \tilde{W}_{\mathbf{R}}^{\alpha_4}(\mathbf{r}')$$

are the matrix elements of *screened* Coulomb interaction $v_{\text{scr}}(\mathbf{r}, \mathbf{r}')$, which are supposed to be diagonal with respect to the site indices $\{\mathbf{R}\}$. The intersite matrix elements are typically small.

Since we do not consider here the relativistic spin-orbit interaction, the matrix elements $t_{\mathbf{R}\mathbf{R}'}^{\alpha_1\alpha_2}$ are diagonal with respect to the spin indices: i.e., $t_{\mathbf{R}\mathbf{R}'}^{\alpha_1\alpha_2} = t_{\mathbf{R}\mathbf{R}'}^{m_1 m_2} \delta_{s_1 s_2}$. The spin-dependence of the screened Coulomb interactions $U_{\alpha_1\alpha_2\alpha_3\alpha_4}^{\mathbf{R}}$ also has the regular form: $U_{\alpha_1\alpha_2\alpha_3\alpha_4}^{\mathbf{R}} = U_{m_1 m_2 m_3 m_4}^{\mathbf{R}} \delta_{s_1 s_2} \delta_{s_3 s_4}$. Generally, the matrix elements of $\hat{U}^{\mathbf{R}} = \|U_{m_1 m_2 m_3 m_4}^{\mathbf{R}}\|$ depend on the site-index \mathbf{R} .

4.1. One-electron part

The one-electron part of the model Hamiltonian (2) can be constructed by using the formal downfolding method, which is applied to the Kohn-Sham equations within LDA. The method has been proposed in [29, 31]. It is totally equivalent to calculation of

the matrix elements of the Kohn-Sham Hamiltonian in the basis of Wannier functions constructed by using the projector-operator technique [32]. The advantage of the downfolding method is that by using it one can formally bypass the construction of the Wannier functions themselves and go directly to the calculation of the one-electron part of the model Hamiltonian. The comparison between original LDA bands and the ones obtained in the downfolding method is shown in figure 3. Generally, the agreement

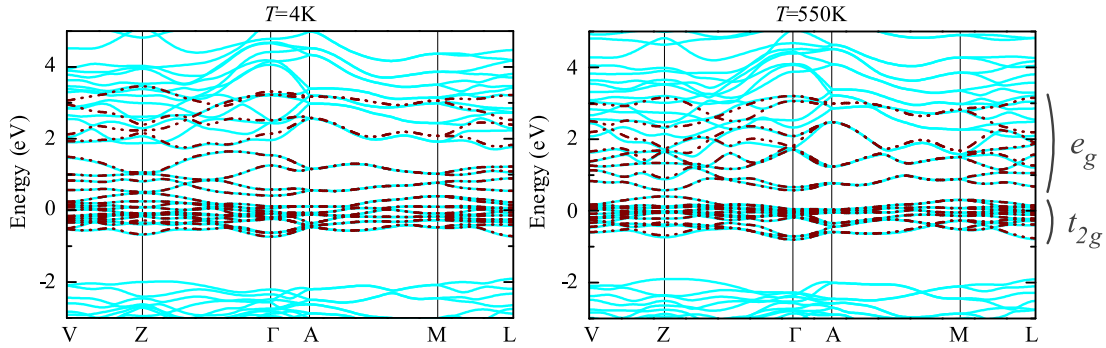


Figure 3. LDA energy bands corresponding to the low-temperature (left) and high-temperature (right) monoclinic structures of BiMnO_3 as obtained in the original electronic structure calculations using LMTO method (solid curves) and after the tight-binding (TB) parametrization using the downfolding method (dash-dotted curves). Notations of the high-symmetry points of the Brillouin zone are taken from [33].

is nearly perfect for the low-energy $\text{Mn}(t_{2g})$ and the first four $\text{Mn}(e_g)$ bands. In this region, the original electronic structure of the LMTO method is well reproduced after the downfolding. However, for the upper $\text{Mn}(e_g)$ bands, which strongly overlap and interact with the $\text{Bi}(6p)$ bands, it is virtually impossible to reproduce all details of the electronic structure in the minimal model consisting only of the $\text{Mn}(3d)$ bands.⁶ Therefore, in the upper-energy region, the electronic structure obtained in the downfolding method is only an approximation to the original LDA band structure.

The model parameters for the one-electron part are obtained after the Fourier transformation of the downfolded Hamiltonian to the real space. In this case, the site-diagonal part of $\hat{t}_{\mathbf{R}\mathbf{R}'} = \|t_{\mathbf{R}\mathbf{R}'}^{m_1 m_2}\|$ describes the crystal-field splitting. The splitting of the e_g levels in the low-temperature phase is particularly strong, being of the order of 1.5 eV (figure 4). As we will see below, the crystal-field effects will lead to a peculiar type of the orbital ordering, which will be mainly responsible for the magnetic properties of BiMnO_3 . This crystal-field splitting is mainly related with the change of the hybridization (or the covalent mixing) in different bonds of the distorted perovskite structure, which after the downfolding gives rise to the site-diagonal contributions in the model Hamiltonian. The nonsphericity of the Madelung potential, which plays a crucial role in the t_{2g} compounds [34, 35], is considerably smaller than the effects of the covalent mixing in the e_g bands and can be neglected. In the high-temperature phase, the crystal-field splitting shrinks

⁶ In the other words, in order to reproduce all bands we had to expand our Wannier basis and treat on an equal footing both $\text{Mn}(3d)$ and $\text{Bi}(6p)$ states.

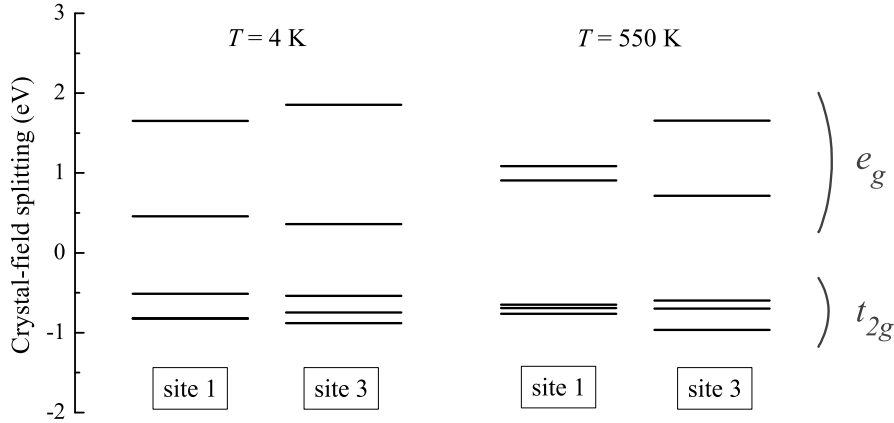


Figure 4. Crystal-field splitting as obtained for the low-temperature (left) and high-temperature (right) monoclinic structures of BiMnO_3 . Positions of the Mn sites are explained in figure 1.

only in one of the sublattices, formed by the Mn atoms ‘1’ and ‘2’ in figure 1. In the second sublattice, formed by the atoms ‘3’ and ‘4’, the e_g -level splitting remains large, being of the order 1 eV.

Because of complexity of the transfer integrals in the monoclinic structure, it is rather difficult to discuss the behavior of individual matrix elements of $\|t_{\mathbf{R}\mathbf{R}'}^{m_1 m_2}\|$. Nevertheless, some useful information can be obtained from the analysis of *averaged* parameters

$$\bar{t}_{\mathbf{R}\mathbf{R}'}(d) = \left(\sum_{m_1 m_2} t_{\mathbf{R}\mathbf{R}'}^{m_1 m_2} t_{\mathbf{R}'\mathbf{R}}^{m_2 m_1} \right)^{1/2},$$

where d is the distance between Mn-sites \mathbf{R} and \mathbf{R}' . All transfer integrals are localized and practically restricted by the nearest neighbors at around 4 Å (figure 5). The longer-range interactions are considerably smaller.

4.2. Screened Coulomb interactions

The matrix elements of screened Coulomb interactions in the Mn(3d) band, $\hat{U}^{\mathbf{R}}$, can be computed in two steps [29, 30]. First, we perform the conventional constrained LDA calculations [36], and derive parameters of the on-site Coulomb interaction $u = 10$ eV and the intraatomic exchange interaction $j = 1$ eV. These parameters are certainly too large and only weakly depend on the crystal environment of Mn-atoms in the solid. They include several important channel of screening: for example, the screening of 3d-interactions by other electrons and the screening caused by relaxation of the atomic 3d wavefunctions are already included in the definition of u and j . However, this is not the whole screening and what the constrained LDA typically cannot do is to treat the so-called self-screening caused *by the same 3d electrons*, which participate in the formation of other bands due to the hybridization effects [30]. The major contribution comes from the O(2p) band, which has a large weight of the Mn(3d) states (figure 2). This channel

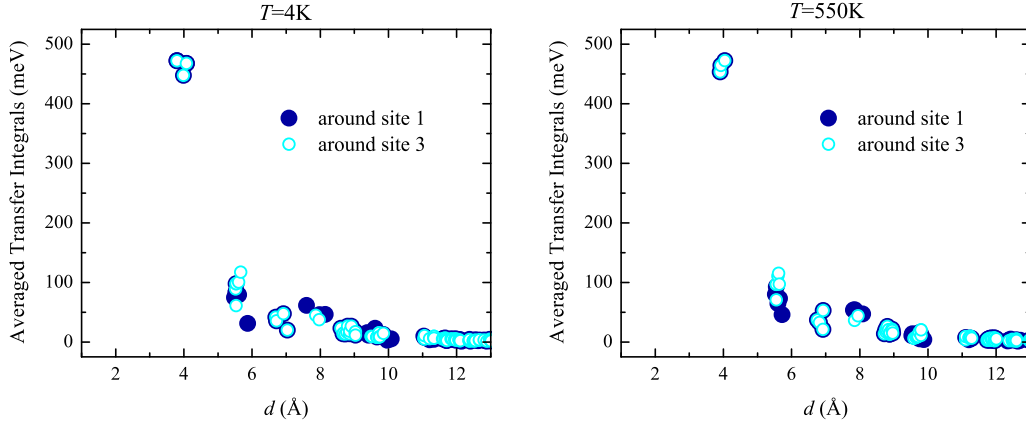


Figure 5. Distance-dependence of averaged transfer integrals, $\bar{t}_{\mathbf{R}\mathbf{R}'}(d) = (\sum_{m_1 m_2} t_{\mathbf{R}\mathbf{R}'}^{m_1 m_2} t_{\mathbf{R}'\mathbf{R}}^{m_2 m_1})^{1/2}$, as obtained for the low-temperature (left) and high-temperature (right) monoclinic structures of BiMnO_3 . The values around two inequivalent Mn sites are shown by closed and open symbols. Positions of the Mn sites are explained in figure 1.

of screening can be efficiently taken into account in the random-phase approximation (RPA) by starting from interaction parameters obtained in the constrained LDA [29]:

$$\hat{U} = [1 - \hat{u}\hat{P}]^{-1} \hat{u},$$

where \hat{P} is the static polarization matrix in RPA, calculated in the basis of atomic $3d$ orbitals,⁷ and \hat{u} is the $5 \times 5 \times 5 \times 5$ matrix of Coulomb interaction in the atomic limit. For each transition-metal site, \hat{u} can be obtained from the parameters u and j by using a regular procedure, which is typically adopted in the LDA+ U method [30]. The polarization matrix \hat{P} is computed by using the LDA band structure. Nevertheless, in order to simulate the electronic structure close to the saturated ferromagnetic ground state, we have used different Fermi levels for the majority- and minority-spin channels in the process of calculation of \hat{P} . Namely, for the minority-spin channel, it was assumed that the Mn($3d$) band is empty and the Fermi level has been placed right after the O($2p$) band (i.e., around -1.5 eV in figure 3), while for the majority-spin channel, it was assumed that the Mn($3d$) band accommodates all sixteen electrons (per four formula units). Meanwhile, we switch off all contributions to the polarization matrix related with the transitions between Mn($3d$) bands in order to get rid of the unphysical metallic screening, which is present in RPA if one starts from the LDA band structure [37].

Then, for each Mn-site, we obtain the $5 \times 5 \times 5 \times 5$ matrix $\hat{U}^{\mathbf{R}}$, which can generally depend on \mathbf{R} and incorporate some effects of the local environment in solids. The symmetry of these matrices is also different from the spherical one. Nevertheless, just for the explanatory purposes, we fit each matrix in terms of three well known

⁷ In the present context, the “atomic orbitals” mean the muffin-tin orbitals of the LMTO method [26, 27, 28].

Table 3. Results of parametrization of screened Coulomb interactions in terms of the on-site Coulomb repulsion U , intraatomic exchange coupling J , and “nonsphericity” B for the low-temperature ($T= 4$ K) and high-temperature ($T= 550$ K) monoclinic phases of BiMnO_3 . All parameters are measured in eV. Positions of the Mn sites are explained in figure 1.

interaction parameters	$T= 4$ K		$T= 550$ K	
	site 1	site 3	site 1	site 3
U	2.27	2.27	2.31	2.22
J	0.89	0.88	0.89	0.88
B	0.09	0.09	0.09	0.09

parameters, which would fully specify all intraatomic interactions between $3d$ electrons in the spherical environment: the Coulomb repulsion $U = F^0$, the intraatomic exchange coupling $J = (F^2 + F^4)/14$, and the “nonsphericity” $B = (9F^2 - 5F^4)/441$, where F^0 , F^2 , and F^4 are radial Slater’s integrals. These parameters have the following meaning: U is responsible for the stability of certain atomic configuration with the given number of electrons, while J and B are responsible for the first and second Hund rule, respectively. The results of such a fitting are shown in table 3. One can clear see that the Coulomb repulsion U is greatly reduced due to the self-screening effects, which are related with the admixture of the $\text{Mn}(3d)$ states into the $\text{O}(2p)$ band.

5. Analysis of the Model Hamiltonian

5.1. Hartree-Fock Approximation

In order to solve the model Hamiltonian (2) we employ the simplest mean-field Hartree-Fock approximation, where the trial many-electron wavefunction is searched in the form of a single Slater determinant $|S\{\varphi_k^s\}\rangle$, constructed from the one-electron orbitals $\{\varphi_k^s\}$. In this notation, k is a collective index combining the momentum \mathbf{k} in the first Brillouin zone and the band number, and s is the spin of the particle. The one-electron orbitals are requested to minimize the total energy

$$E_{\text{HF}} = \min_{\{\varphi_k^s\}} \langle S\{\varphi_k^s\} | \hat{\mathcal{H}} | S\{\varphi_k^s\} \rangle \quad (3)$$

for a given number of particles \mathcal{N} . The minimization is equivalent to the solution of Hartree-Fock equations for $\{\varphi_k^s\}$:

$$\left(\hat{t}_{\mathbf{k}} + \hat{\mathcal{V}}^s \right) |\varphi_k^s\rangle = \varepsilon_k^s |\varphi_k^s\rangle, \quad (4)$$

where $\hat{t}_{\mathbf{k}} \equiv \|t_{\mathbf{k}}^{m_1 m_2}\|$ is the one-electron part of the model Hamiltonian (2) in the reciprocal space, $t_{\mathbf{k}}^{m_1 m_2} = \sum_{\mathbf{R}, \mathbf{R}'} t_{\mathbf{R} \mathbf{R}'}^{m_1 m_2} e^{-i\mathbf{k} \cdot (\mathbf{R} - \mathbf{R}')}$, and $\hat{\mathcal{V}}^s \equiv \|\mathcal{V}_{\mathbf{R} m_1 m_2}^s\|$ is the Hartree-Fock potential,

$$\mathcal{V}_{\mathbf{R} m_1 m_2}^\dagger = \sum_{m_3 m_4} \left\{ U_{m_1 m_2 m_3 m_4}^{\mathbf{R}} \left(n_{\mathbf{R} m_3 m_4}^\uparrow + n_{\mathbf{R} m_3 m_4}^\downarrow \right) - U_{m_1 m_4 m_3 m_2}^{\mathbf{R}} n_{\mathbf{R} m_3 m_4}^\uparrow \right\} \quad (5)$$

(similar equation for $\mathcal{V}_{\mathbf{R}m_1m_2}^\downarrow$ is obtained by interchanging \uparrow and \downarrow). Equations (4) are solved self-consistently together with the equation

$$\hat{n}^s = \sum_k^{occ} |\varphi_k^s\rangle \langle \varphi_k^s|$$

for the density matrix $\hat{n}^s \equiv \|n_{\mathbf{R}m_1m_2}^s\|$ in the basis of Wannier functions.

After self-consistency, the total energy (3) can be computed as

$$E_{\text{HF}} = \sum_{ks}^{occ} \varepsilon_k^s - \frac{1}{2} \sum_{\mathbf{R}s} \sum_{m_1m_2} \mathcal{V}_{\mathbf{R}m_2m_1}^s n_{\mathbf{R}m_1m_2}^s.$$

5.2. Magnetic Interactions

By knowing $\{\varepsilon_k\}$ and $\{\varphi_k\}$, one can construct the one-electron (retarded) Green function,

$$\hat{\mathcal{G}}_{\mathbf{R}\mathbf{R}'}^s(\omega) = \sum_k \frac{|\varphi_k^s\rangle \langle \varphi_k^s|}{\omega - \varepsilon_k^s + i\delta} e^{i\mathbf{k} \cdot (\mathbf{R} - \mathbf{R}')},$$

which can be used in many applications. For example, the interatomic magnetic interactions corresponding to infinitesimal rotations of the spin magnetic moments near the equilibrium can be easily computed as [38, 39]:

$$J_{\mathbf{R}\mathbf{R}'} = \frac{1}{2\pi} \text{Im} \int_{-\infty}^{\varepsilon_F} d\omega \text{Tr}_L \left\{ \hat{\mathcal{G}}_{\mathbf{R}\mathbf{R}'}^\uparrow(\omega) \Delta \hat{\mathcal{V}}_{\mathbf{R}'} \hat{\mathcal{G}}_{\mathbf{R}'\mathbf{R}}^\downarrow(\omega) \Delta \hat{\mathcal{V}}_{\mathbf{R}} \right\}, \quad (6)$$

where $\Delta \hat{\mathcal{V}}_{\mathbf{R}} = \hat{\mathcal{V}}_{\mathbf{R}}^\uparrow - \hat{\mathcal{V}}_{\mathbf{R}}^\downarrow$ is the magnetic (spin) part of the Hartree-Fock potential, Tr_L denotes the trace over the orbital indices, and ε_F is the Fermi energy. According to (6), $J_{\mathbf{R}\mathbf{R}'} > 0$ (< 0) means that for the given magnetic state, the spin alignment in the bond $\langle \mathbf{R}\mathbf{R}' \rangle$ corresponds to the local minimum (maximum) of the total energy. However, in the following we will use the universal notations, according to which $J_{\mathbf{R}\mathbf{R}'} > 0$ and < 0 will stand the ferromagnetic and antiferromagnetic coupling, respectively. These notations correspond to the mapping of the total energy change of the Hartree-Fock method, associated with the small rotations of the magnetic moments, onto the Heisenberg model [38]:

$$E_{\text{Heis}} = -\frac{1}{2} \sum_{\mathbf{R}\mathbf{R}'} J_{\mathbf{R}\mathbf{R}'} \mathbf{e}_{\mathbf{R}} \cdot \mathbf{e}_{\mathbf{R}'},$$

where $\mathbf{e}_{\mathbf{R}}$ is the direction of the spin magnetic moment at the site \mathbf{R} .

Generally, the parameters $\{J_{\mathbf{R}\mathbf{R}'}\}$ are not universal and depend on the magnetic state in which they are calculated (for example, through the change of the orbital ordering [35] or the electronic structure [40] in each magnetic state).

If we are dealing with the collinear magnetic structure, where all spins are parallel to the z -axis, i.e. $\mathbf{e}_{\mathbf{R}} = (0, 0, 1)$ or $(0, 0, -1)$, one can consider a small rotation of the magnetic moment at one of the site, $\mathbf{e}_{\mathbf{R}} = (\cos \theta_{\mathbf{R}} \sin \phi_{\mathbf{R}}, \sin \theta_{\mathbf{R}} \sin \phi_{\mathbf{R}}, \cos \theta_{\mathbf{R}})$, and calculate the second derivative of E_{Heis} with respect to $\theta_{\mathbf{R}}$:

$$J_{\mathbf{R}}^0 = \sum_{\mathbf{R}'} s_{\mathbf{R}\mathbf{R}'} J_{\mathbf{R}\mathbf{R}'} \quad (7)$$

In this expression, $s_{\mathbf{R}\mathbf{R}'} = 1$ and -1 stands correspondingly for the FM and AFM alignment in the bond $\langle \mathbf{R}\mathbf{R}' \rangle$. $J_{\mathbf{R}}^0$ characterizes the stability of the magnetic system with respect to the rotation of the single spin. It can be also related with the spin stiffness and the magnetic transition temperature in the mean-field approximation [38]. If $J_{\mathbf{R}}^0 > 0$, the spin system is stable while if $J_{\mathbf{R}}^0 < 0$ it is unstable.

5.3. Decomposition into “Double Exchange” and “Superexchange”

Many properties of perovskite manganese oxides are related with the simple fact that the exchange splitting $\Delta\hat{\mathcal{V}}_{\mathbf{R}}$ is large, and for many applications can be treated as the largest parameter in the problem [40, 41]. This is because Mn^{3+} ions have four unpaired $3d$ electrons, which interact through the Hund’s rule coupling J . Loosely speaking, the exchange splitting between the majority and minority spin states is controlled by the parameter $U+3J$, which is about 4.9 eV (table 3), whereas the orbital polarization (or the splitting of occupied states with one particular projection of spin) is controlled by $U-J$, being “only” about 1.4 eV. Therefore, as the first approximation, one can neglect the orbital dependence of $\Delta\hat{\mathcal{V}}_{\mathbf{R}}$ and replace it by some constant exchange splitting Δ_{ex} : i.e.,

$$\Delta\mathcal{V}_{\mathbf{R}mm'} \rightarrow \Delta_{\text{ex}}\delta_{mm'}. \quad (8)$$

A typical example of the exchange splitting in the low-temperature monoclinic phase is shown in figure 6: the averaged exchange splitting Δ_{ex} is about 4.7 eV, whereas the

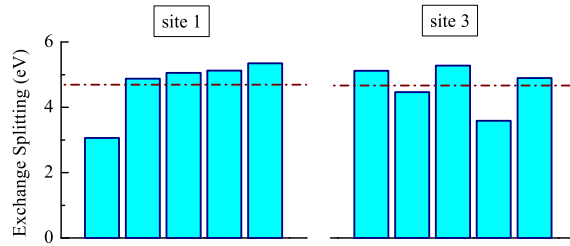


Figure 6. Diagonal matrix elements of the exchange splitting for five d orbitals in the low-temperature monoclinic phase. The off-diagonal matrix elements are considerably smaller. The dash-dotted line shows the averaged value of the exchange splitting (approximately 4.7 eV). Positions of the Mn sites are explained in figure 1.

deviations from Δ_{ex} for the particular orbitals do not exceed 1.5 eV. Of course, (8) is a crude approximation. Nevertheless, as will see below, it appears to be very useful for the analysis of interatomic magnetic interactions. It also reproduces the main trends of the behavior of these interactions at least on the semi-quantitative level.

Since Δ_{ex} is large, all minority-spin states are empty (figure 7). Therefore, all poles of $\hat{\mathcal{G}}_{\mathbf{R}'\mathbf{R}}^\downarrow$ are located in the unoccupied part of the spectrum and below ε_{F} one can use the $1/\Delta_{\text{ex}}$ expansion for $\hat{\mathcal{G}}_{\mathbf{R}'\mathbf{R}}^\downarrow$ [40, 41]. Then, the first two terms in the expansion of

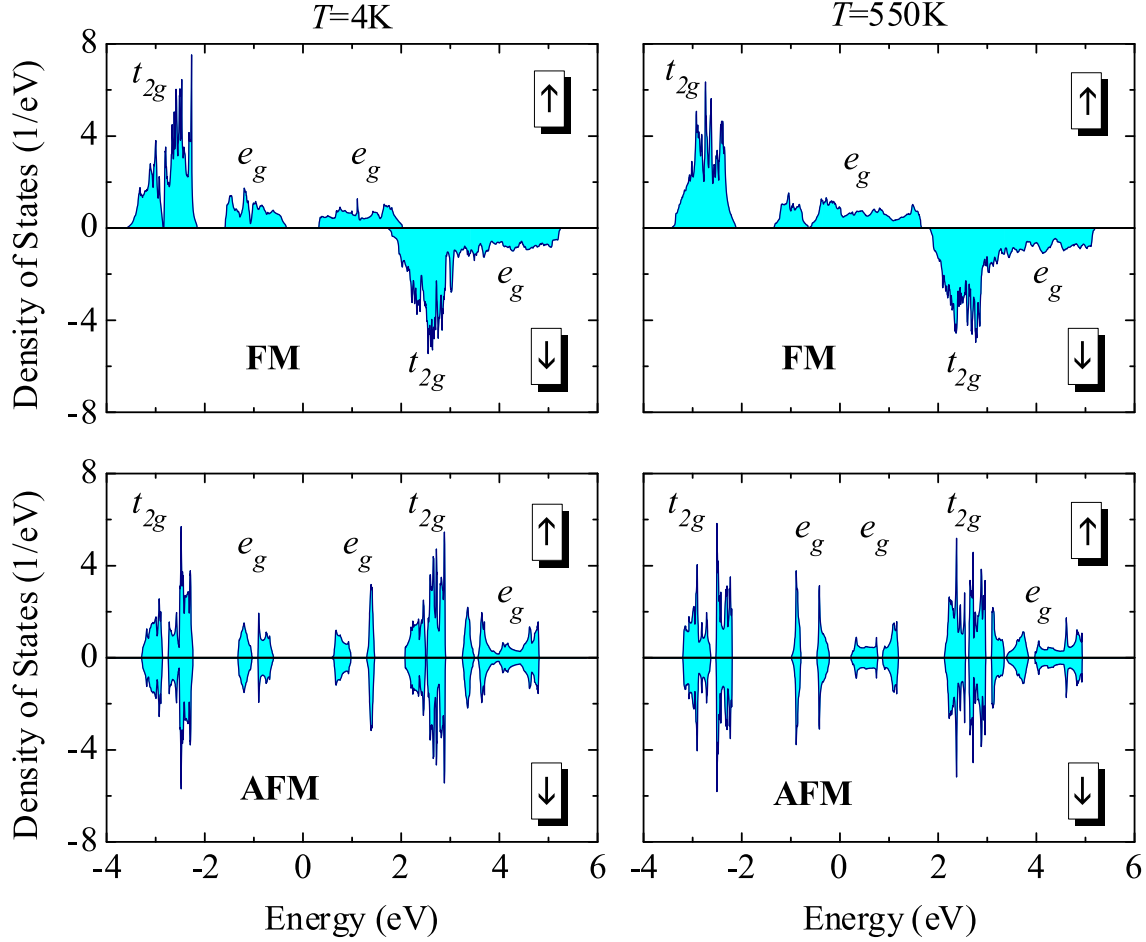


Figure 7. Density of states in the ferromagnetic (top) and antiferromagnetic $\uparrow\downarrow\uparrow$ (bottom) phases of BiMnO_3 , as obtained in the Hartree-Fock calculations using low-temperature (left) and high-temperature (right) monoclinic structures. The Fermi level is at zero energy (shown by dash-dotted line). Symbols show positions of the main bands.

$J_{\mathbf{R}\mathbf{R}'}$ will have the following from:

$$J_{\mathbf{R}\mathbf{R}'}^D = -\frac{1}{2\pi} \text{Im} \int_{-\infty}^{\epsilon_F} d\omega \text{Tr}_L \left\{ \hat{\mathcal{G}}_{\mathbf{R}\mathbf{R}'}^{\uparrow}(\omega) \hat{h}_{\mathbf{R}'\mathbf{R}} \right\}, \quad (9)$$

and

$$J_{\mathbf{R}\mathbf{R}'}^S = -\frac{1}{2\pi\Delta_{\text{ex}}} \text{Im} \int_{-\infty}^{\epsilon_F} d\omega \text{Tr}_L \left\{ \hat{\mathcal{G}}_{\mathbf{R}\mathbf{R}'}^{\uparrow}(\omega) \left(2\omega \hat{h}_{\mathbf{R}'\mathbf{R}} + (\hat{h}_{\mathbf{R}'\mathbf{R}})^2 \right) \right\}, \quad (10)$$

where we have used the notations $\hat{h}_{\mathbf{R}'\mathbf{R}} = \hat{t}_{\mathbf{R}'\mathbf{R}} + \hat{\mathcal{V}}_{\mathbf{R}}^{\uparrow} \delta_{\mathbf{R}'\mathbf{R}}$ and $(\hat{h}_{\mathbf{R}'\mathbf{R}})^2 = \sum_{\mathbf{R}''} \hat{h}_{\mathbf{R}'\mathbf{R}''} \hat{h}_{\mathbf{R}''\mathbf{R}}$.

$J_{\mathbf{R}\mathbf{R}'}^D$ is proportional to $\{\hat{t}_{\mathbf{R}'\mathbf{R}}\}$ and does not depend on Δ_{ex} . In an analogy with [40, 41], we will call it “the double exchange interaction”, although, strictly speaking, it is not a regular double exchange since $\hat{\mathcal{G}}_{\mathbf{R}\mathbf{R}'}^{\uparrow}$ also includes $\hat{\mathcal{V}}_{\mathbf{R}}^{\uparrow}$, which takes into accounts the effects of the orbital polarization of the electronic origin. $J_{\mathbf{R}\mathbf{R}'}^S$ incorporates the effects of the second order with respect to $\{\hat{t}_{\mathbf{R}'\mathbf{R}}\}$ and is inversely proportional to Δ_{ex} . Therefore, in the following it will be called “the superexchange interaction”. We will

also consider two approximation for $J_{\mathbf{R}\mathbf{R}'}^D$ and $J_{\mathbf{R}\mathbf{R}'}^S$. In the first one, $\hat{h}_{\mathbf{R}'\mathbf{R}}$ will be regular Hartree-Fock Hamiltonian for the majority-spin states and $\hat{\mathcal{G}}_{\mathbf{R}\mathbf{R}'}^\uparrow$ is the Green function corresponding to this Hamiltonian:

$$\hat{\mathcal{G}}_{\mathbf{R}\mathbf{R}'}^\uparrow = \left[\omega - \hat{h} + i\delta \right]_{\mathbf{R}\mathbf{R}'}^{-1}. \quad (11)$$

In the second one, in order to be consistent with the approximate expression (8) for the exchange splitting, we will neglect all effects of the orbital polarization of the electronic origin also in the definition of $\hat{h}_{\mathbf{R}'\mathbf{R}}$ and $\hat{\mathcal{G}}_{\mathbf{R}\mathbf{R}'}^\uparrow$. Therefore, apart from the constant shift, $\hat{h}_{\mathbf{R}'\mathbf{R}}$ is replaced by $\hat{t}_{\mathbf{R}'\mathbf{R}}$. Then, $\hat{\mathcal{G}}_{\mathbf{R}\mathbf{R}'}^\uparrow$ is the regular LDA Green function, which is obtained from (11) after replacing \hat{h} by \hat{t} . In this approximation, it becomes more clear why we continue to use the term “double exchange”, even though our system can be insulating, like the low-temperature phase of BiMnO_3 , where already in LDA there is a gap between $\text{Mn}(e_g)$ bands (figure 3). It is true that the existence of this gap, Δ , is related with some kind of the orbital polarization. In this sense it is still reasonable to consider the superexchange processes by treating all transfer integrals as a perturbation. This would correspond to the superexchange interactions of the form t_{eff}^2/Δ , where t_{eff}^2 is the square of an effective transfer integral between Mn sites, which is related with $\{\hat{t}_{\mathbf{R}'\mathbf{R}}\}$. However, this orbital polarization comes from the large crystal-field splitting, which is just another effect of the covalent mixing, and, therefore has the same origin as t_{eff} . Therefore, Δ should be proportional to t_{eff} , and the “superexchange” t_{eff}^2/Δ becomes also proportional to t_{eff} . From this point of view, it is still reasonable to call this interaction as the “double exchange”.

6. Results and Discussion

The orbital ordering in the low-temperature monoclinic phase of BiMnO_3 is shown in figure 8. We have tried three different methods in order to derive the distribution of the electron density around Mn-sites.

- (i) In the first method, we simply calculate the site-diagonal elements of the density matrix in the original LMTO basis by integrating over four lowest e_g bands (spreading around 1 eV in figure 3), and plot the electron density corresponding to this density matrix.
- (ii) In the second method, we plot the densities of the lowest e_g -orbitals obtained from the diagonalization of the site-diagonal part of the one-electron Hamiltonian, which was derived from the downfolding method. In the other words, these are just the crystal-field orbitals, corresponding to the fourth atomic level in figure 4.
- (iii) In the third method, we plot the electron density for the occupied \uparrow -spin e_g band, obtained in the Hartree-Fock calculations for the ferromagnetic state (figure 7).

All three methods provide a very consistent picture for the general details of the orbital ordering in the low-temperature phase of BiMnO_3 , which is also consistent with results of full-potential calculations by Shishidou [20].

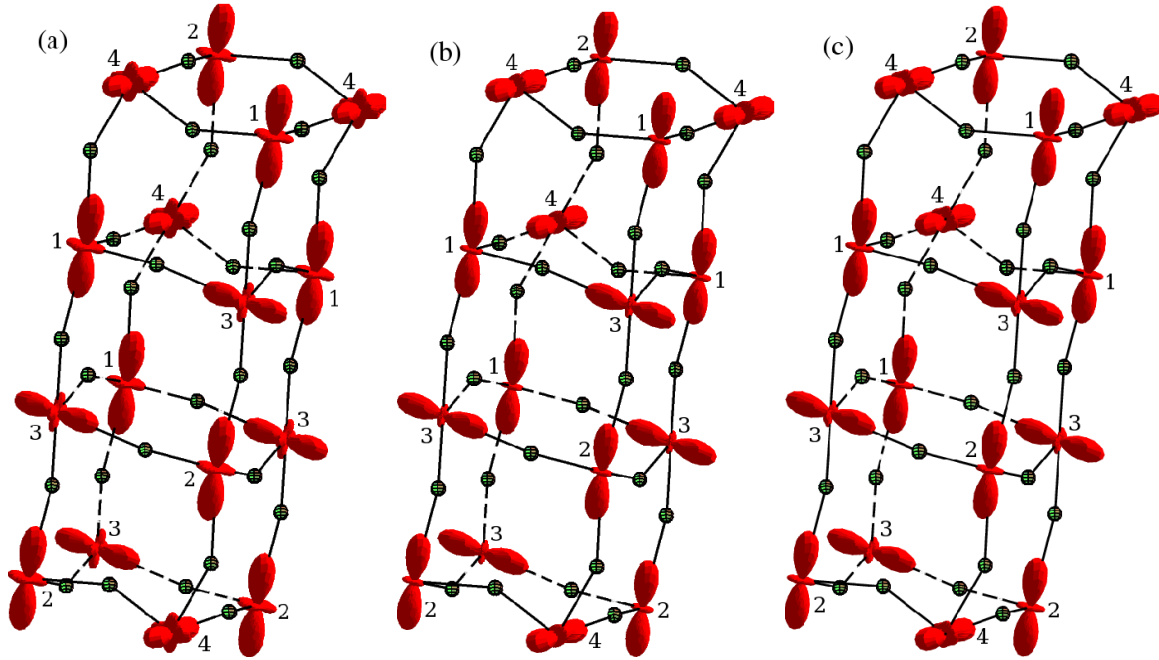


Figure 8. Orbital ordering in the low-temperature monoclinic phase of BiMnO_3 obtained through the site-diagonal elements of the density matrix in the original LMTO basis (a), through the crystal-field orbitals of downfolded Hamiltonian (b), and through the density matrix derived in Hartree-Fock calculations for the ferromagnetic state (c). Four types of Mn atoms are indicated by the numbers.

The orbital ordering in the high-temperature structure, derived from the crystal-field orbitals, is shown in figure 9. This orbital ordering is entirely related with the crystal distortion, which splits the atomic e_g levels. Even for the sites ‘1’ and ‘2’ with the least distorted environment (table 4), this splitting is of the order of 0.2 eV. This corresponds to the temperature of about 2100 K, which largely exceeds the temperature of monoclinic-to-orthorhombic transition (about 770 K [14]). Thus, it is reasonable to expect the orbital ordering to take place in *both* monoclinic phases, below and above 474 K. However, as it is clearly seen from the comparison of figures 8 and 9, the character of the orbital ordering will change at the point of phase transition. This conclusion is qualitatively consistent with results of resonant x-ray scattering on BiMnO_3 [42].

Results of Hartree-Fock calculations of the total energies for the ferromagnetic and several antiferromagnetic configurations are shown in table 4. Our main observation is that for the low-temperature monoclinic structure the ferromagnetic phase appears to be nearly degenerate with the antiferromagnetic $\uparrow\downarrow\uparrow\downarrow$ phase, which can be obtained by flipping the directions of the magnetic moments at the Mn-sites ‘2’ and ‘3’. Perhaps, the tendencies towards the antiferromagnetism are somewhat overestimated in our model, and there are several reasons for it:

- (i) The calculations of the Coulomb interaction U are always conjugated with certain approximations [29, 30], and some of these parameters may be underestimated. As we will see below, larger values of the parameter U would indeed help in stabilizing

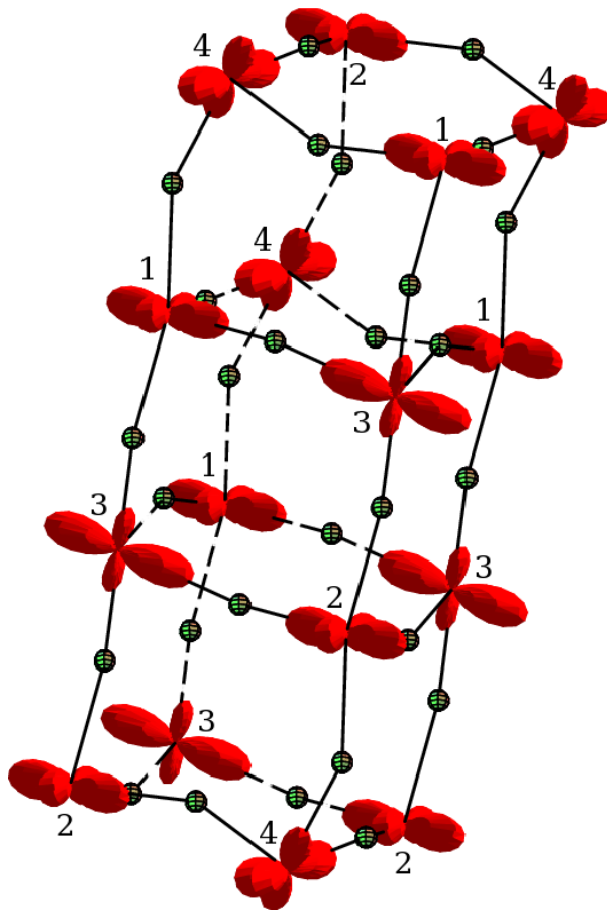


Figure 9. Orbital ordering in the high-temperature monoclinic structure of BiMnO_3 . Four types of Mn atoms are indicated by the numbers.

Table 4. Total energies for several antiferromagnetic configurations as obtained in the Hartree-Fock calculations for the low-temperature ($T = 4$ K) and high-temperature ($T = 550$ K) monoclinic structures of BiMnO_3 . The energies measured in meV per one formula unit relative to the ferromagnetic state.

configuration	$T = 4$ K	$T = 550$ K
$\uparrow\downarrow\uparrow\uparrow$	-0.5	9.4
$\uparrow\uparrow\downarrow\downarrow$	19.0	48.4
$\uparrow\downarrow\downarrow\downarrow$	3.9	28.4
$\downarrow\downarrow\uparrow\downarrow$	5.6	21.5

the ferromagnetic phase.

- (ii) Our model (2) does not explicitly include the oxygen states. This appears to be a good approximation for titanium and vanadium perovskite oxides [35], where the transition-metal and oxygen bands are well separated. However, manganese compounds are much closer to the charge-transfer regime because of the proximity of $\text{Mn}(3d)$ and $\text{O}(2p)$ bands, and much stronger hybridization, which takes place between these groups of states. Moreover, as it was pointed out in section 4.1, there

is also an overlap between $\text{Mn}(3d)$ and $\text{Bi}(6p)$ bands. Therefore, the Hubbard model (2), where the form of the Coulomb interactions is borrowed from the atomic limit for the $\text{Mn}(3d)$ states is an approximation, which may ignore some contributions to the relative stability of different magnetic configurations. For example, it is known that the magnetic polarization of the oxygen states will additionally stabilize the FM phase [43]. These effects are not included into the model (2).

Nevertheless, as we will see below, the competition between ferromagnetic and antiferromagnetic $\uparrow\downarrow\uparrow$ phases itself is a genuine effect, which is directly related with the form of the orbital ordering in the low-temperature monoclinic structure.

The distance-dependence of interatomic magnetic interactions calculated in the low-temperature monoclinic structure is shown in figure 10. These calculations have been

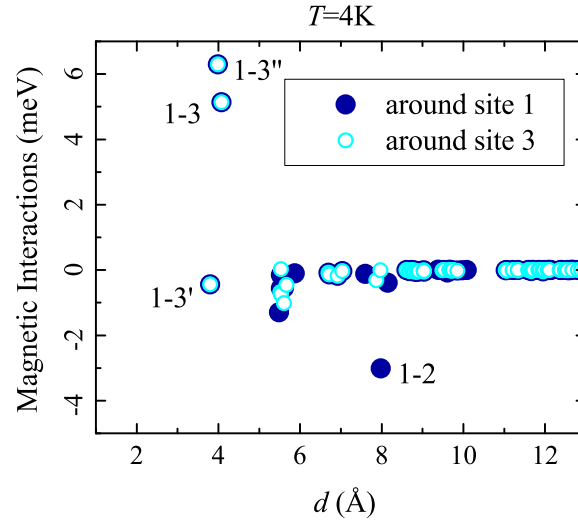


Figure 10. Distance-dependence of interatomic magnetic interactions in the low-temperature monoclinic structure of BiMnO_3 . The values around two inequivalent Mn sites are shown by closed and open symbols. Other notations indicate the bonds for the most relevant magnetic interactions. Positions of the Mn sites are explained in figures 1 and 11.

performed using the formula (6) for infinitesimal rotations of magnetic moments near the ferromagnetic state. We note the following. There are two types of relatively strong ferromagnetic interactions between nearest neighbors, which operate in the bonds 1-3 and 1-3'' (see figure 11 for notations).⁸ The character of these interactions is directly related with the “antiferromagnetic” orbital ordering in the bonds 1-3 and 1-3'', and can be anticipated already from distribution of the Mn-O bondlengths in the low-temperature monoclinic phase [5].⁹ The interaction in the third bond 1-3', formed by the

⁸ Since in the ferromagnetic structure, the atoms 3 and 4 can be transformed to each other by the symmetry operations, similar interactions hold between atoms 1 and 4. However, for the sake of clarity, we do not show all these bonds in figure 11.

⁹ In the present context, the “antiferromagnetic orbital ordering” means nearly orthogonal orientation of occupied e_g orbitals, which maximizes the electron hoppings into the unoccupied subspace and,

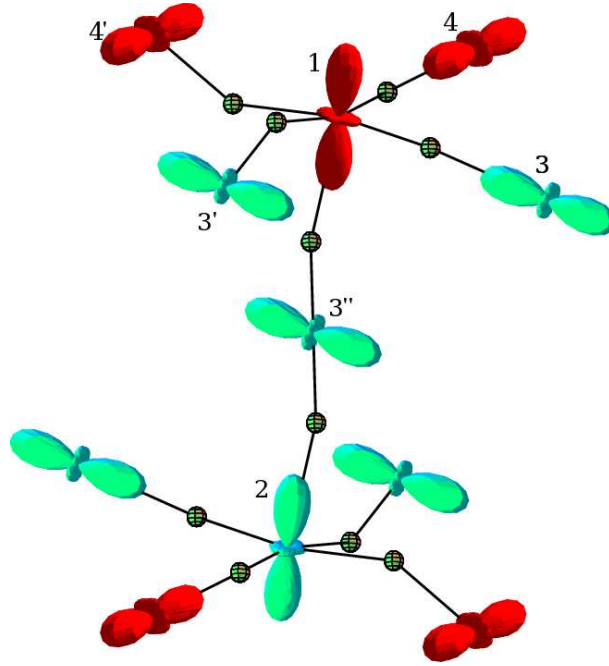


Figure 11. Fragment of the orbital ordering pattern in the low-temperature monoclinic phase of BiMnO_3 . Different magnetic sublattices, which are formed in the antiferromagnetic $\uparrow\downarrow\uparrow$ structure are shown by different colors.

nearest neighbors, is relatively weak. This is again consistent with the geometry of the orbital ordering, corresponding to the minimal overlap between occupied and unoccupied e_g orbitals. Similar situation occurs in the bond 1-4'. The most striking result of the present calculations is the existence of relatively strong long-range antiferromagnetic interaction in the bond 1-2 (figure 11). Nevertheless, this result is also anticipated from the geometry of the orbital ordering. Note that the occupied e_g orbitals at the sites 1 and 2 are directed towards each other. Although the direct transfer integrals between these two sites are relatively small (see figure 5), it is still reasonable to expect the existence of AFM interactions, which are mediated by unoccupied e_g states of the site 3''. Such a situation is somewhat similar to superexchange interactions, which take place via oxygen states in the charge-transfer insulators [45, 46], and the mechanism itself is sometimes called as the “super-superexchange”.

Thus, in the low-temperature monoclinic phase of BiMnO_3 we are always dealing with a competition of nearest-neighbor FM and longer-range AFM interactions. In fact, there are several factors, which can make these interactions comparable with each other. It is true that, generally, the nearest-neighbor interactions are expected to be much stronger, because all transfer integrals are basically restricted by the nearest neighbors (figure 5). However, for the nearest-neighbor interactions we are also dealing with the strong cancellation of FM “double exchange” and AFM superexchange contributions (table 5). For example, this cancellation is nearly perfect for the “weak bonds” 1-3' and therefore, favors the ferromagnetic interactions between these sites [44].

Table 5. Magnetic interactions in ferromagnetic (FM) and antiferromagnetic (AFM) $\uparrow\downarrow\uparrow$ phases as obtained for the low-temperature ($T = 4$ K) and high-temperature ($T = 550$ K) monoclinic structures. The columns ‘DE’ and ‘SE’ show results of (approximate) decomposition into double exchange and superexchange contribution using electronic structure obtained in the Hartree-Fock calculations for the ferromagnetic state and the one in LDA (in the parenthesis). All values are in meV. Positions of Mn sites are explained in figure 11.

bond	$T = 4$ K				$T = 550$ K		
	FM	AFM	DE	SE	FM	DE	SE
1-3	5.1	1.7	32.9 (42.0)	-30.1 (-29.5)	15.9	43.2	-30.3
1-4	5.1	7.8	32.9 (42.0)	-30.1 (-29.5)	15.9	43.2	-30.0
1-3'	-0.4	-1.0	16.5 (22.4)	-20.4 (-21.7)	19.2	40.6	-24.0
1-4'	-0.4	0.7	16.5 (22.4)	-20.4 (-21.7)	19.2	40.6	-24.0
1-3''	6.3	5.1	29.8 (36.8)	-26.3 (-26.0)	18.5	41.7	-26.2
2-3''	6.3	5.6	29.8 (36.8)	-26.3 (-26.0)	18.5	41.7	-26.2
1-2	-3.0	-3.0	-0.5 (-0.7)	-1.4 (-1.7)	1.0	1.4	0.2

1-4'. This is a general rule for perovskite manganese oxides, which explains a strong reduction of nearest-neighbor magnetic interactions, so that they can easily become comparable with some longer-range interactions [39, 40, 41]. On the other hands, for the longer-range AFM interaction in the bond 1-2, there is no such cancellation. The long-range interactions are expected to vanish for the undoped (parent) manganites, provided that they would have a undistorted cubic structure. This effect is entirely related with the symmetric filling (or half-filling) of the majority-spin e_g band [41]. Nevertheless, many parent manganites (like BiMnO_3) have a strongly distorted crystal structure. This distortion gives rise to the orbital ordering, which leads to certain asymmetry of filling of the majority-spin e_g band, and this asymmetry is finally manifested in the appearance of longer-range interactions.

Since nearest-neighbor interactions favor the ferromagnetism, while the longer-range interactions favor the formation of the antiferromagnetic $\uparrow\downarrow\uparrow$ structure, one can generally expect the competition between these two phases, as it is clearly seen from results of total energy calculations shown in table 4. Nevertheless, there is another factor, which will additionally stabilizes the AFM $\uparrow\downarrow\uparrow$ phase and explains why it is so close in energy to the FM phase.

Note that the orbital degrees of freedom can additionally change their form in order to modify the interatomic magnetic interactions in the direction which will further stabilize the given magnetic structure [44]. Since the form of the orbital ordering is efficiently constrained by the large crystal-field splitting, it does not strongly depend on the magnetic state, and visually one can observe only tiny changes in the distribution of occupied e_g electron density (figure 12). Nevertheless, it is interesting to see that these tiny changes may have a profound effect on the behavior of interatomic magnetic

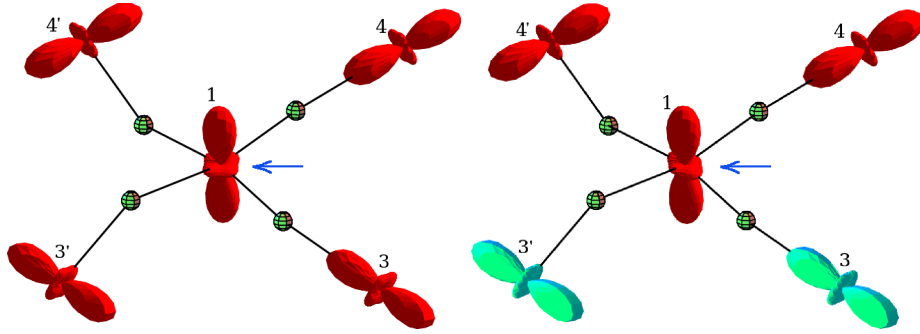


Figure 12. Details of orbital ordering in the ferromagnetic (left) and antiferromagnetic (right) phases realized in the low-temperature monoclinic structure of BiMnO_3 . Different magnetic sublattices are shown by different colors. The arrow shows the region where the change of the orbital cloud results in the drastic change of interatomic magnetic interactions.

interactions. Indeed, in the AFM $\uparrow\downarrow\uparrow$ structure, the chain 1-3''-2 contains one AFM bond (1-3'') and one FM bond (2-3'', see figure 11). Although in the AFM structure, both interactions remain ferromagnetic, there is a clear *polarity* of interactions and the magnetic coupling in the AFM bond 1-3'' is considerably weaker than the one in the ferromagnetic bond 2-3'' (table 5). Even more dramatic change occurs in the plane of the distorted perovskite structure. In the AFM structure, even visually one can see some anisotropy in distribution of the occupied e_g electron density at the site 1 (figure 12), which appears to be more contracted in the direction of the FM bond 1-4. On the other hand, this distribution is nearly isotropic in the FM phase. This means that in the direction 1-4 of the AFM phase, the weight of the e_g orbitals is additionally moved into the unoccupied part of the spectrum. This opens some additional pathes for the virtual hoppings into the unoccupied part of the spectrum, which will additionally stabilize the FM coupling. Indeed, the exchange coupling in the FM bond 1-4 is 7.8 meV, while the one in the AFM bond 1-3 is strongly reduced till 1.7 meV. Moreover, the magnetic interactions in the weak bonds 1-3' and 1-4' are also adjusted by the orbital-ordering effects. For example, the AFM coupling in the bond 1-3' is enhanced, while the coupling in the FM bond 1-4' becomes ferromagnetic.

Because of these orbital ordering effects both magnetic configurations appear to be locally stable. Indeed, the parameters $J_{\mathbf{R}}^0$, calculated in the FM and AFM $\uparrow\downarrow\uparrow$ phases are (7.4, 12.1) and (17.6, 8.9) meV, respectively, where the first number in parenthesis corresponds to the Mn-site 1, while the second number corresponds to the Mn-site 3. All parameters are positive, meaning that both configurations are stable, at least with respect to independent rotations of magnetic moments at the sites 1 and 3.

In addition to electronic degrees of freedom, the AFM $\uparrow\downarrow\uparrow$ phase can be additionally stabilized by structural effects associated with polar atomic displacements in the direction which further minimizes the total energy of the system via magneto-elastic interactions. For example, magnetic couplings in the bonds 1-3'' and 2-3'' can be further adjusted by displacement of the Mn-atom 3'' (figure 11). Although we do not

consider such a mechanism here (that would require detailed structural optimization using modern full-potential electronic structure methods), it would be certainly an interesting step to do in the future. This mechanism was considered for example in [25, 24] for other multiferroic compounds.

In the high-temperature monoclinic structure, the FM phase is clearly the most stable one (table 4). This is closely related with the fact that the FM phase is metallic (figure 7) and the double exchange interactions clearly dominate (table 5). However, this is true only for the low-temperature regime. At elevated temperatures, the structure of interatomic magnetic interactions will be largely modified by the magnetic disorder, which may also destroy metallic character of the electronic structure.¹⁰ Thus, it is rather meaningless to discuss the properties of the high-temperature phase in the low-temperature limit. The magnetic disorder in the high-temperature phase is certainly one of the interesting problems. However, it is beyond the scopes of the present work. The possible tools to address this problem is the coherent potential approximation (CPA) [47, 48], or, more generally, the dynamical mean-field theory (DMFT) [49]. Nevertheless, we would like to emphasize that since the type of the orbital ordering changes above 474 K (figure 9), the long-range interactions between atoms 1 and 2 are expected to be weak. Therefore, the long-range AFM correlations, which according to our point of view are indispensable for the inversion symmetry breaking and appearance of the ferroelectricity, should not play any important role in the high-temperature monoclinic phase. Thus, according to our scenario, the temperature of the isostructural phase transition (474 K) should be also regarded as a upper bound for the possible onset of ferroelectricity.

7. Implications to the Properties of BiMnO_3

Thus, we would like to propose that the multiferroic behavior of BiMnO_3 should be closely related with a competition between two magnetic phases. One is the centrosymmetric (and antiferroelectric) FM phase. Another one is the AFM $\uparrow\downarrow\uparrow$ phase, which breaks the inversion symmetry and allows for the spontaneous electric polarization in the direction perpendicular to the y -axis. The existence of both phases is closely related with the peculiar orbital ordering, which takes place below 474 K.

This means that despite the fact that BiMnO_3 is crystallized in the centrosymmetric $C2/c$ structure, there is still a room for the multiferroic behavior, if we could engineer the samples where these two phases coexist in a narrow energy range accessible for the physical changes of electric and magnetic fields as well as the temperature T . Then, one could readily expect the “switching phenomena”. For example, by applying the magnetic field H one could stabilize the FM antiferroelectric phase and switch off the net electric polarization. Conversely, one could apply the electric field E and stabilize the AFM ferroelectric phase with zero net magnetization.

¹⁰ In fact, the Hartree-Fock calculations for the high-temperature monoclinic structure shown that only the FM phase is metallic, whereas all considered AFM phases are insulating (figure 7).

It is true the low-temperature ferromagnetism in the pure bulk samples of BiMnO_3 is well established today [5]. Therefore, the symmetry is expected to be $C2/c$ and these samples are not extremely promising from the viewpoint of multiferroic applications. However, it is also known that the BiMnO_3 is extremely difficult to synthesize, especially in the single crystalline form. Therefore, it is reasonable to expect that the BiMnO_3 samples will always have some defects, and we would like to speculate that these defects may play a positive role in stabilizing some fractions of antiferromagnetic and noncentrosymmetric phase. This seems to be reasonable, because the low-temperature magnetization observed in the BiMnO_3 samples, which do exhibit the ferroelectric behavior, was only $2.6\mu_B$ and reached $3.1\mu_B$ per one formula unit in high magnetic fields [12]. These values are considerably lower than $4\mu_B$ expected for the single saturated FM phase, meaning that the samples were not sufficiently pure and might contain a fraction of the AFM phase. This strongly reminds the idea of clustering or macroscopic phase separation, which has been intensively discussed in other perovskite manganese oxides, in the context of colossal magnetoresistance phenomena [50, 51].

In this respect it is important to note that even in the high-quality samples, whose low-temperature saturation magnetization was close to $4\mu_B$ [5], the authors of [17] and [52], by means of atomic pair distribution function analysis on neutron powder diffraction data and selected-area electron diffraction technique, respectively, have observed the existence of short-range ordered structures (or domains) with the broken inversion symmetry. The symmetry of these structures was either $P2$ or $P2_1$, which is consistent with the crystal symmetry of the AFM $\uparrow\downarrow\downarrow\uparrow$ phase ($P2$), that we propose. Moreover, these experimental data strongly suggests that the breaking of the inversion symmetry is mainly caused by the Mn atoms, that is again consistent with the idea of the magnetic origin of this effect. Unfortunately, the authors of [17, 52] focused only on the structural properties of BiMnO_3 , and did not provide any information on how these structural properties can be related with the magnetic behavior of BiMnO_3 . From our point of view, such measurements would be very useful. For example, if the origin of the noncentrosymmetric domains was indeed magnetic, it is reasonable to expect the size and relative weight of these domains to decrease in the magnetic field.

Another possibility to control the properties of BiMnO_3 is to use the thin films. In this case, due to the lattice mismatch of the bulk BiMnO_3 and the substrate, the latter causes an additional strain and may strongly affect the magnetic behavior of BiMnO_3 . This effect is well known for other (colossal magnetoresistive) manganese oxides, and can be used as an efficient tool for controlling the electronic and magnetic properties of these systems near the point of phase transition between FM and AFM states [53, 54]. Moreover, the magnetic structure at the surface of BiMnO_3 may be also different from the one in the bulk. Indeed, the saturation magnetization of the BiMnO_3 thin films grown on the (100) SrTiO_3 substrate was only $2.8\mu_B$ [55], which is considerably smaller than the bulk value. The magnetic moment increases almost linearly with the increases of the film thickness and reaches the nearly saturated value at around 500 Å. The use of the (110) SrTiO_3 substrate yields even smaller saturation moment (about $1.8\mu_B$

[55]). Thus, all these data suggest that the magnetic ground state realized in the thin films of BiMnO_3 is not a pure FM one, and may contain some elements of the AFM structure. Of course, on the basis of this highly limited experimental information about the saturation magnetization it is impossible to make a ultimate conclusion whether this AFM structure is indeed the $\uparrow\downarrow\downarrow\uparrow$ one, which we propose. Nevertheless, one can speculate that the ferroelectric behavior, which is apparently seen in the BiMnO_3 thin films, can be again related with the deviation of the magnetic structure from the pure FM one [12, 15].

Finally, although the ground state of BiMnO_3 is ferromagnetic, some fraction of the AFM $\uparrow\downarrow\downarrow\uparrow$ phase can emerge at elevated temperatures. If at zero temperature both FM and $\uparrow\downarrow\downarrow\uparrow$ AFM phases correspond to the local minima of the total energy and are connected to each other by the first-order transition, the rising of the temperature can naturally lead to a coexistence of these two states. By neglecting the interaction between two phases, this effects is simply related with the configuration mixing entropy. Moreover, the appearance of the two-phase state is considerably facilitated in the presence of defects [50, 51], as it is well known for other (colossal magnetoresistive) manganites [56]. This behavior implies the existence of the temperature hysteresis loop in the magnetization curve near T_C . A small temperature hysteresis has been indeed reported in [5], which may be related with small anomalies of dielectric constant observed in [14]. Since the existence of the long-range AFM interaction is closely related with the peculiar orbital ordering persisting up to 474 K, no ferroelectricity can be generally expected above this temperature.

In summary, we believe that further exploration of multiferroic behavior of BiMnO_3 should be focused on the revealing of the AFM $\uparrow\downarrow\downarrow\uparrow$ phase. Possible multiferroic applications of BiMnO_3 will strongly depend on whether one can find the conditions of coexistence of the FM and AFM $\uparrow\downarrow\downarrow\uparrow$ phases in a narrow energy range accessible for the switching by electric and magnetic fields. It seems that the available experimental data do not rule out this idea, although at the present stage there is no direct support to it either. We hope that our work will stimulate theoretical and experimental activity in this direction.

Acknowledgments

We are grateful to Alexei Belik for stimulating our interest to the problem of magnetism and orbital ordering in BiMnO_3 , numerous discussions, and providing us unpublished structure parameters of BiMnO_3 at 4K. We are also grateful to Tatsuya Shishidou for discussions of unpublished results of his electronic structure calculations for BiMnO_3 . The work of IVS is partly supported by Grant-in-Aid for Scientific Research in Priority Area “Anomalous Quantum Materials” and Grant-in-Aid for Scientific Research (C) No. 20540337 from the Ministry of Education, Culture, Sport, Science and Technology of Japan. The work of ZVP is partly supported by Dynasty Foundation, Grants of President of Russia MK-3227.2008.2, and scientific school grant SS-1929.2008.2.

References

- [1] Fiebig M 2005 *J. Phys. D: Appl. Phys.* **38** R123
- [2] Khomskii D I 2006 *J. Magn. Magn. Matter.* **306** 1
- [3] Eerenstein W, Mathur N D and Scott J F 2006 *Nature* **442** 759
- [4] Cheong S-W and Mostovoy M 2007 *Nature materials* **6** 13
- [5] Belik A A, Iikubo S, Yokosawa T, Kodama K, Igawa N, Shamoto S, Azuma M, Takano M, Kimoto K, Matsui Y and Takayama-Muromachi E 2007 *J. Am. Chem. Soc.* **129** 971
- [6] Chiba H, Atou T, Syono Y 1997 *J. Solid State Chem.* **132** 139
- [7] Hill N A and Rabe K M 1999 *Phys. Rev. B* **59** 8759
- [8] Seshadri R and Hill N A 2001 *Chem. Mater.* **13** 2892
- [9] Atou T, Chiba H, Ohoyama K, Yamaguchi Y and Syono Y 1999 *J. Solid State Chem.* **145** 639
- [10] Moreira dos Santos A, Cheetham A K, Atou T, Syono Y, Yamaguchi Y, Ohoyama K, Chiba H and Rao C N R 2002 *Phys. Rev. B* **66** 064425
- [11] Montanari E, Calestani G, Migliori A, Dapiaggi M, Bolzoni F, Cabassi R and Gilioli Ed 2005 *Chem. Mater.* **17** 6457
- [12] Moreira dos Santos A, Parashar S, Raju A R, Zhao Y S, Cheetham A K and Rao C N R 2002 *Solid State Commun.* **122** 49
- [13] Shishidou T, Mikamo N, Uratani Y, Ishii F and Oguchi T 2004 *J. Phys.: Condens. Matter* **16** S5677
- [14] Kimura T, Kawamoto S, Yamada I, Azuma M, Takano M and Tokura Y (2003) *Phys. Rev. B* **67** 180401(R)
- [15] Sharan A, Lettieri J, Jia Y, Tian W, Pan X, Schlom D G, and Gopalan V 2004 *Phys. Rev. B* **69** 214109
- [16] Montanari E, Calestani G, Righi L, Gilioli E, Bolzoni F, Knight K S and Radaelli P G (2007) *Phys. Rev. B* **75** 220101(R)
- [17] Yokosawa T, Belik A A, Asaka T, Kimoto K, Takayama-Muromachi E and Matsui Y 2008 *Phys. Rev. B* **77** 024111
- [18] Eerenstein W, Morrison F D, Sher F, Prieto J L, Attfield J P, Scott J F, Mathur N D 2007 *Phil. Mag. Lett.* **87** 249
- [19] Belik A A, Iikubo S, Kodama K, Igawa N, Shamoto S, Maie M, Nagai T, Matsui Y, Stefanovich S Yu, Lazoryak B I and Takayama-Muromachi E 2006 *J. Am. Chem. Soc.* **128** 706
- [20] Shishidou T 2007 *private communication*
- [21] Baettig P, Seshadri R and Spaldin N A 2007 *J. Am. Chem. Soc.* **129** 9854
- [22] Belik 2007 *private communication*
- [23] Sergienko I A, Şen C and Dagotto E 2006 *Phys. Rev. Lett.* **97** 227204
- [24] Picozzi S, Yamauchi K, Sanyal B, Sergienko I A and Dagotto E 2007 *Phys. Rev. Lett.* **99** 227201
- [25] Wang C, Guo G-C and He L 2007 *Phys. Rev. Lett.* **99** 177202
- [26] Andersen O K 1975 *Phys. Rev. B* **12** 3060
- [27] Gunnarsson O, Jepsen O and Andersen O K 1983 *Phys. Rev. B* **27** 7144
- [28] Andersen O K and Jepsen O 1984 *Phys. Rev. Lett.* **53** 2571
- [29] Solovyev I V 2006 *Phys. Rev. B* **73** 155117
- [30] Solovyev I V 2008 *J. Phys.: Condens. Matter* (to be published)
- [31] Solovyev I V 2004 *Phys. Rev. B* **69** 134403
- [32] Solovyev I V, Pchelkina Z V and Anisimov V I 2007 *Phys. Rev. B* **75** 045110
- [33] Bradley C J and Cracknell A P 1972 *The Mathematical Theory of Symmetry in Solids* (Oxford: Clarendon Press)
- [34] Mochizuki M and Imada M 2003 *Phys. Rev. Lett.* **91** 167203
- [35] Solovyev I V 2006 *Phys. Rev. B* **74** 054412
- [36] Gunnarsson O, Andersen O K, Jepsen O and Zaanen J 1989 *Phys. Rev. B* **39** 1708
- [37] Aryasetiawan F, Imada M, Georges A, Kotliar G, Biermann S and Lichtenstein A I 2004 *Phys.*

- Rev. B* **70** 195104
- [38] Liechtenstein A I, Katsnelson M I, Antropov V P and Gubanov V A 1987 *J. Magn. Magn. Matter.* **67** 65
- [39] Solovyev I V 2003 Magnetic Interactions in Transition-Metal Oxides *Recent Research Developments in Magnetism and Magnetic Materials* (India: Transworld Research Network) vol 1 p 253
- [40] Solovyev I V and Terakura K 2003 Orbital Degeneracy and Magnetism of Perovskite Manganese Oxides (*Electronic Structure and Magnetism of Complex Materials*), ed D J Singh and D A Papaconstantopoulos (Berlin: Springer) p 253
- [41] Solovyev I V and Terakura K 1999 *Phys. Rev. Lett.* **82** 2959
- [42] Yang C-H, Koo J, Song C, Koo T Y, Lee K-B and Jeong Y H 2006 *Phys. Rev. B* **73** 224112
- [43] Mazurenko V V, Skornyakov S L, Kozhevnikov A V, Mila F and Anisimov V I 2007 *Phys. Rev. B* **75** 224408
- [44] Kugel K I and Khomskii D I 1982 *Sov. Phys. Usp.* **25** 231
- [45] Oguchi T, Ketarura K and Williams A R 1983 *Phys. Rev. B* **28** 6443
- [46] Zaanen J and Sawatzky G A 1987 *Can. J. Phys.* **65** 1262
- [47] de Brito P E and Shiba H 1998 *Phys. Rev. B* **57** 1539
- [48] Solovyev I V 2003 *Phys. Rev. B* **67** 014412
- [49] Georges A, Kotliar G, Krauth W and Rozenberg M J 1996 *Rev. Mod. Phys.* **68** 13
- [50] Nagaev E L 1996 *Physics - Uspekhi* **39** 781
- [51] Dagotto E 2005 *New J. Phys.* **7** 67
- [52] Kodama K, Iikubo S, Shamoto S-i, Belik A A and Takayama-Muromachi E 2007 *J. Phys. Soc. Jpn.* **76** 124605
- [53] Konishi Y, Fang Z, Izumi M, Manako T, Kasai M, Kuwahara H, Kawasaki M, Terakura K and Tokura Y 1999 *J. Phys. Soc. Jpn.* **68** 3790
- [54] Fang Z, Solovyev I V and Terakura K 2000 *Phys. Rev. Lett.* **84** 3169
- [55] Ohshima E, Saya Y, Nantoh M and Kawai M 2000 *Solid State Commun.* **116** 73
- [56] Uehara M, Mori S, Chen C H and Cheong S-W 1999, *Nature* **399** 560